The Astrophysical Journal, 956:83 (13pp), 2023 October 20 https://doi.org/10.3847/1538-4357/ace621

Quantifying Poynting Flux in the Quiet Sun Photosphere

Dennis Tilipman[1,2], Maria Kazachenko[1,2], Benoit Tremblay[3], Ivan Milić[4,5], Valentin Martínez Pillet[1], and Matthias Rempel[3]
[1] National Solar Observatory, University of Colorado Boulder, Boulder, CO, USA; dennis.tilipman@colorado.edu
[2] Department of Astrophysical and Planetary Sciences, University of Colorado Boulder, Boulder, CO, USA
[3] High Altitude Observatory, National Center for Atmospheric Research, Boulder, CO, USA
[4] Leibniz Institute for Solar Physics (KIS), Freiburg, Germany
[5] Faculty of Mathematics, University of Belgrade, Belgrade, Serbia
Received 2023 March 2; revised 2023 June 6; accepted 2023 July 2; published 2023 October 10

Abstract

Poynting flux is the flux of magnetic energy, which is responsible for chromospheric and coronal heating in the solar atmosphere. It is defined as a cross product of the electric and magnetic fields, and in ideal MHD conditions it can be expressed in terms of the magnetic field and plasma velocity. Poynting flux has been computed for active regions and plages, but estimating it in the quiet Sun (QS) remains challenging due to resolution effects and polarimetric noise. However, with the upcoming DKIST capabilities, such estimations will become more feasible than ever before. Here, we study QS Poynting flux in SUNRISE/IMaX observations and MURaM simulations. We explore two methods for inferring transverse velocities from observations—FLCT and a neural network–based method DeepVel—and show DeepVel to be the more suitable method in the context of small-scale QS flows. We investigate the effect of azimuthal ambiguity on Poynting flux estimates, and we describe a new method for azimuth disambiguation. Finally, we use two methods for obtaining the electric field. The first method relies on an idealized Ohm's law, whereas the second is a state-of-the-art inductive electric field inversion method PDFI_SS. We compare the resulting Poynting flux values with theoretical estimates for chromospheric and coronal energy losses and find that some of the Poynting flux estimates are sufficient to match the losses. Using MURaM simulations, we show that photospheric Poynting fluxes vary significantly with optical depth, and that there is an observational bias that results in underestimated Poynting fluxes due to an unaccounted shear term contribution.

Unified Astronomy Thesaurus concepts: The Sun (1693); Solar physics (1476); Solar atmosphere (1477); Solar photosphere (1518); Solar chromospheric heating (1987)

1. Introduction

Quantitative estimates of vertical energy transport in the solar photosphere have been limited, yet they are explicitly relevant to many observed phenomena on the Sun, including flux emergence (Cheung & Isobe 2014; Afanasyev et al. 2021), chromospheric and coronal heating (Withbroe & Noyes 1977; Vernazza et al. 1981), and solar flares and coronal mass ejections (Tziotziou et al. 2013; Kazachenko et al. 2015; Pomoell et al. 2019). The flux of magnetic energy, i.e., the Poynting flux or Poynting vector, defined as the cross product of the electric and magnetic fields, has long been considered a primary mechanism for energy transport from the photosphere to the overlying atmosphere, but specific magnetically driven processes and their relative importance have remained somewhat elusive (Steiner et al. 2008; Liu & Schuck 2012; Shelyag et al. 2012; Welsch & Fisher 2016). Typically, the flux of magnetic energy is divided into emergence and shear terms. The emergence term arises from the advection of magnetic field lines by upward plasma flows, and the shear term (also called the wave term) is associated with the twisting of field lines by horizontal flows.

Quantitative investigations of photospheric Poynting flux are a relatively recent development, owing to the fact that the intermediate quantities needed to compute it—full electric and magnetic field vectors—are difficult to obtain even from modern state-of-the-art observations. Significant strides have been made in both magnetic field inversions from observed Stokes profiles (Asensio Ramos & Díaz Baso 2019; de la Cruz Rodríguez 2019), and electric field inversions (e.g., Welsch & Fisher 2016; Fisher et al. 2020). However, most of the quantitative studies of Poynting flux have been constrained to either simulated data (Shelyag et al. 2012; Kazachenko et al. 2014; Afanasyev et al. 2021; Breu et al. 2022, 2023), or active regions and plages (Kazachenko et al. 2015; Lumme et al. 2019), since in these settings one deals with relatively high polarimetric signal-to-noise ratios (S/Ns). In particular, Breu et al. (2022) used high-fidelity simulations of the quiet Sun (QS) photosphere to explain heating in a coronal loop, while Kazachenko et al. (2015) computed Poynting flux from Active Region 11158 and found it to be sufficient to explain the heating of the chromosphere and corona, according to theoretical estimates in Withbroe & Noyes (1977). However, an analogous, observation-based study into Poynting flux in the QS has not been conducted. Yeates et al. (2014) and Welsch (2014) put constraints on the coronal energy associated with motions of photospheric footpoints and plages, but they used an ideal MHD formulation of Ohm's law and they assumed zero upward advective motion, thereby neglecting the emergence term of Poynting flux. More recently, Silva et al. (2022) produced quantitative estimates of QS Poynting flux, but their focus was mostly on the horizontal flux and their method also included several simplifications, such as an idealized Ohm's law and reliance on apparent motions of magnetic field

concentrations to obtain velocities transverse to the line of sight (LOS; i.e., parallel to the plane of the sky).

Studies of magnetic features in the QS have been few and far between due to both the noisiness of observations and systematic issues. The SUNRISE/IMaX balloon-borne probe provides some of the best currently available QS polarimetry (Martínez Pillet et al. 2011), yet even in this data sample, strong linearly polarized light constitutes only about 10% of the field of view (FOV; Kianfar et al. 2018). Furthermore, there is the outstanding problem of magnetic field 180° azimuthal ambiguity, wherein spectropolarimetric inversions of Stokes profiles return two mathematically valid configurations of the transverse magnetic field. While many methods of disambiguation have been proposed (for a review of some of them and their respective limitations, see, e.g., Pevtsov et al. 2021), none of them have been validated on QS magnetograms. Since a full magnetic vector is necessary to compute Poynting flux, the task of disambiguation is necessary as well.

As a result of these observational and methodological challenges, quantitative investigations into Poynting flux in the QS have been limited. At the same time, there will soon be unprecedented observations of the QS from the Daniel K. Inouye Solar Telescope (DKIST), which will allow us to improve significantly on the spatial resolution, cadence, and/or polarimetric sensitivity (Rimmele et al. 2020). There are also sophisticated methods of computing Poynting flux that have not yet been tested on QS data. This presents a gap in the current state of this discipline, which this paper seeks to fill. Since the QS constitutes the majority of the observed photosphere area-wise, it is imperative that we understand the energy flux from it. The goal of this paper is to compute Poynting flux in the QS photosphere. To this end, we use several methods and we apply them to both observational and simulated data, with a focus on the former.

The remainder of the paper is structured as follows: In Section 2 we describe the observational and simulated data we use in this work, and in Section 3 we explain how we obtain the Poynting flux and the necessary intermediate quantities—full velocity, magnetic field, and electric field vectors. In Section 4 we describe the Poynting flux estimates from the various employed methods, and in Section 5 we discuss them. Finally, in Section 6 we summarize our findings and outline some of the possible future work.

2. Data

2.1. Observational Data: IMaX

We perform our analysis on spectropolarimetric observations from the Imaging Magnetograph Experiment (IMaX) instrument on board the SUNRISE balloon-borne observatory (Martínez Pillet et al. 2011). We use one continuous SUNRISE/IMaX time series taken on 2009 June 9 between 01:30:54 and 02:02:29 UT. This data set covers a 40×40 Mm region of the QS at the disk center and includes a slowly evolving region of relatively high (>200 G, for filling factor unity) magnetic field concentration seen at the bottom of the V Stokes vector map in panels (e)–(h) of Figure 1. The photon S/N of 1000, cadence of 33.25 s, and sampling resolution of $0\farcs0545$ px^{-1} make the IMaX data set the best available source for the purposes of studying Poynting flux in the QS. With this combination of cadence and spatial resolution, a typical flux element moving at a moderate speed of 3 km s^{-1} in the plane of the sky (see, e.g., Asensio Ramos et al. 2017) would traverse two pixels.

IMaX provides high-quality, diffraction-limited polarimetric observations of the QS in the Fe I 5250.2 Å line, which is sensitive to photospheric magnetic fields. The observations include the full Stokes vector (I, Q, U, and V) sampled in five wavelength positions, ±40 and ±80 mÅ on either side of the Fe I 5250.2 Å line and +227 Å in the continuum, with spectral resolution of 65 mÅ (85 mÅ Gaussian). The IMaX Fabry–Perot sensor introduces a systematic blueshift, which grows as a function of distance from the center of the FOV. We apply a correction in the form of a distance-to-center-dependent redshift to account for this effect on the LOS velocity. The level 0 data are also corrected to minimize instrumental effects, such as by dark-frame correction, flat-fielding, and removal of dust-induced effects, resulting in nonreconstructed (NR) data (Martínez Pillet et al. 2011). The Q and U noise levels in the NR data set are estimated to be $8.3 \times 10^{-4} I_c$ and $1.1 \times 10^{-3} I_c$, respectively (Jafarzadeh et al. 2014). In addition, the IMaX point-spread function is used to apply phase diversity reconstruction (PDR) to the NR data, thereby increasing spatial resolution to $0\farcs15$ at the expense of increasing the Q and U noise levels to $2.6 \times 10^{-3} I_c$ and $3.6 \times 10^{-3} I_c$, respectively (Kianfar et al. 2018). We use the NR data, with their lower polarimetric noise, for magnetic field inversions, and the PDR data, with their higher spatial resolution, for velocity inversions.

2.2. Simulation Data: STAGGER

STAGGER (Magic et al. 2013) is a 3D radiative magneto-hydrodynamic (MHD) code that solves for the conservation of mass, energy, and momentum equations. These equations are coupled with the radiative transfer equations in a local thermodynamic equilibrium non-gray atmosphere on a 48 km grid. The simulation cadence is 60 s. We use continuum intensities and transverse velocities from STAGGER simulations of the QS to validate velocities obtained with Fourier local correlation tracking (FLCT) and the neural network based method DeepVel, which are discussed further in Section 3.2.1.

2.3. Simulation Data: MURaM

MURaM (Vögler et al. 2005; Rempel 2014, 2017) is a state-of-the-art radiative MHD code used to model a variety of features in the solar atmosphere and below. The MURaM code solves for mass and energy transfers between the subsurface convective zone and the photosphere, chromosphere, and corona. The simulation we analyze here is based on the case "O16bM" from Rempel (2014) and is extended in the vertical direction by about 500 km. The simulation solves for all the main MHD quantities (magnetic and velocity vectors, temperature, pressure, and heat and energy fluxes) in a domain with a physical extent of $24.576 \times 24.576 \times 8.192$ Mm^3, with an isotropic grid spacing of 16 km, resulting in a $1536 \times 1536 \times 512$ grid. It spans optical depths within approximately $5 \times 10^{-8} < \tau < 10^9$, i.e., from the convection zone to the upper chromosphere and transition region. The location $\tau = 1$ is found about 2 Mm beneath the top boundary. The relevant simulation quantities from the QS MURaM simulation (LOS velocity, $|B|$, S_z, and S_h) are shown in Figure 2.

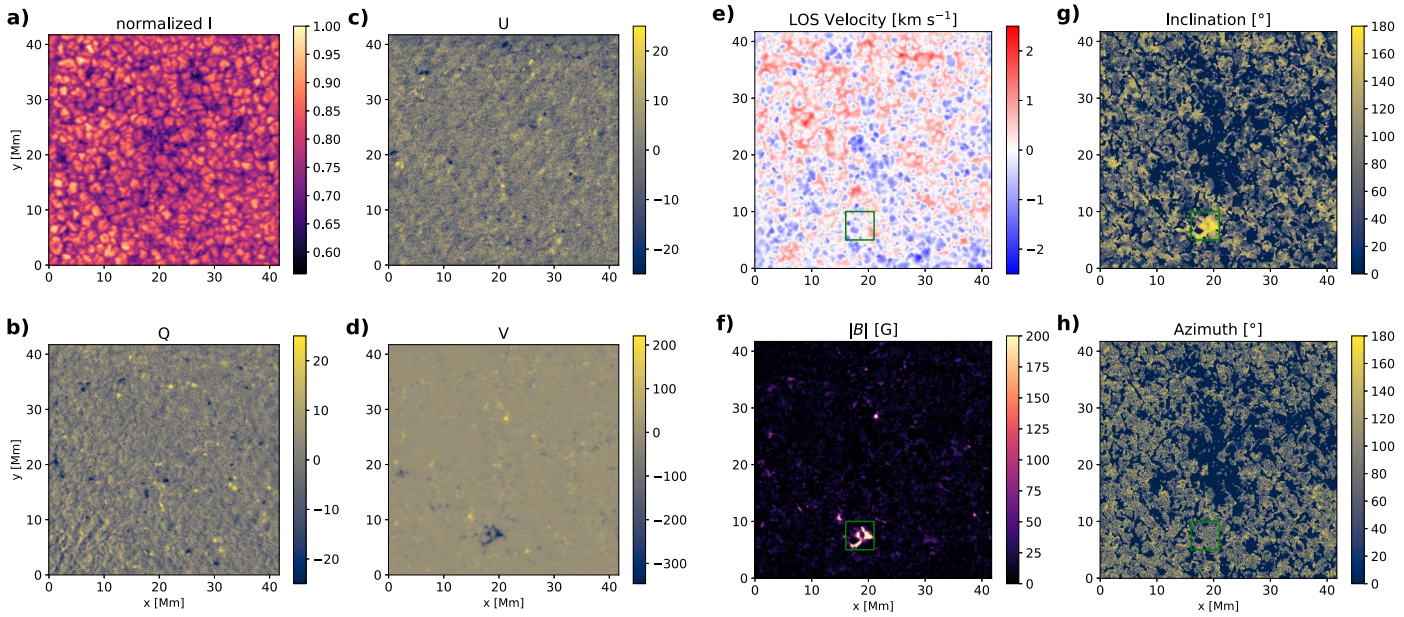

Figure 1. Left panels, (a)–(d): IMaX Stokes vector maps at $t = 1430$ s. Right panels, (e)–(h): IMaX magnetogram and LOS velocity map derived using Milne–Eddington inversions. For the LOS velocity, a correction is applied to account for the systematic bias introduced by the IMaX Fabry–Perot sensor. The bias scales as a function of distance from the FOV center. The green square in the four right panels (e)–(h) outlines the region of interest (ROI), which contains the strongest magnetic field concentration. A close-up view of the ROI is shown in Figure 4. See Section 3.1.1 for a detailed discussion. The full FOV is 836 × 836 pixels, the ROI is 100 × 100 pixels, and each pixel is 48 km across.

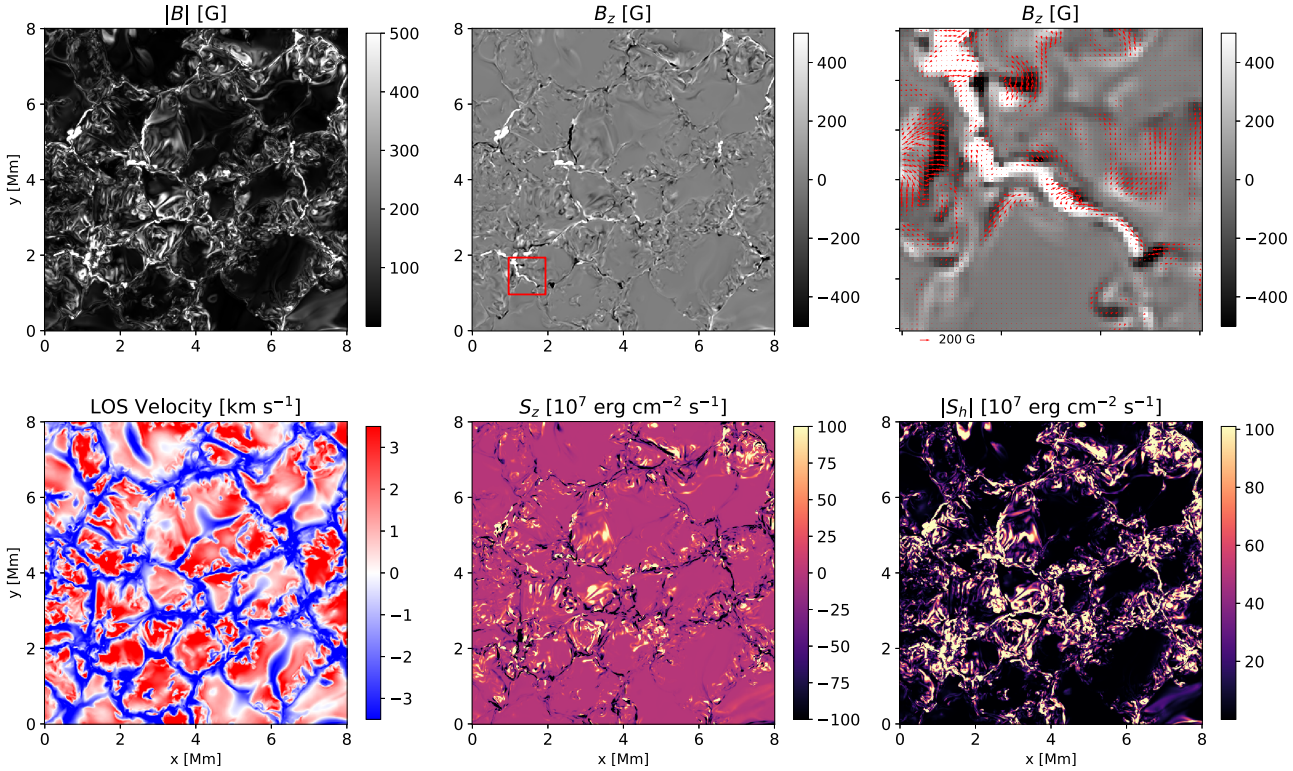

Figure 2. Outputs of a MURaM simulation at the geometrical surface $z = 0$, which corresponds to optical depth $\overline{\tau} = 1.1$, averaged over the FOV. The top right panel is a blowup of the red square in the top center panel. Arrows represent the orientation of transverse magnetic fields. The vertical and horizontal Poynting fluxes S_z and S_h are computed using the ideal MHD method (for details, see Section 3).

3. Methodology

Recall that Poynting flux is defined as

$$\boldsymbol{S} = \frac{1}{4\pi}\boldsymbol{E} \times \boldsymbol{B}, \tag{1}$$

where $\boldsymbol{B}$ and $\boldsymbol{E}$ are the magnetic and electric field vectors, respectively. In Section 3.1, we first describe how we use the polarimetric observations to infer the magnetic field $\boldsymbol{B}$ in the QS. In Section 3.1.1, we summarize the three methods we use to disambiguate the azimuth of the horizontal magnetic field:

the ME0 (Leka et al. 2009b), azimuth randomization, and Poynting flux optimization methods. Finally, in Section 3.2, we review the two approaches we use to derive the electric field $\boldsymbol{E}$: the PDFI_SS electric field inversion method, which solves Faraday's induction equation

$$-\nabla \times \boldsymbol{E} = \frac{\partial \boldsymbol{B}}{\partial t}, \tag{2}$$

and the simplified electric field inversion method, which strictly imposes the idealized Ohm's law

$$\boldsymbol{E} = -\boldsymbol{v} \times \boldsymbol{B}, \tag{3}$$

where $\boldsymbol{v}$ is the velocity vector. In the simplified formulation of Poynting flux, where the idealized Ohm's law is imposed strictly, we can express the vertical Poynting flux (S_z) as follows:

$$S_z = \frac{1}{4\pi}[v_z B_h^2 - (\boldsymbol{v}_h \cdot \boldsymbol{B}_h) B_z], \tag{4}$$

where the z and h subscripts denote vertical and transverse variables, respectively. In this expression, the first term is the emergence term and the second is the wave, or shear, term. In Section 3.2.1, we describe the two transverse velocity reconstruction methods DeepVel and FLCT, since transverse velocities are a required intermediate quantity for using either of the electric field inversions. For brevity, we refer to the simplified approach as the "ideal MHD" method and to the PDFI_SS method as the "inductive method." We emphasize, however, that both approaches could enforce the ideal MHD condition, albeit to different extents: the "ideal MHD" method does so strictly but the "inductive method" does not, though it could enforce it via ideal noninductive contribution (see Section 2.4 in Kazachenko et al. 2014).

3.1. Magnetic Field Inversions

To obtain the magnetic field configuration and LOS velocity from level 1 IMaX polarimetry, we apply the Milne–Eddington inversion code pyMilne (de la Cruz Rodríguez 2019) to the NR IMaX data set. We choose this method for its relative computational efficiency—the assumptions of a Milne–Eddington atmosphere simplify the inversion scheme while adequately capturing the physics of photospheric Fe I 5250.2 Å line formation. For each IMaX frame, the inversion code uses several seeds (`nRandom` parameter) to prevent the scheme from converging to local minima, and several Levenberg–Marquardt iterations (`nIter`) per seed. It should be noted that pyMilne assumes a magnetic filling factor of unity, which may introduce bias in transverse magnetic field inversions (Leka et al. 2022).

We show an example of level 1 Stokes data in panels (a)–(d) in Figure 1 and the corresponding outputs of Milne–Eddington inversions in panels (e)–(h). Clearly visible is the high-V signal region at the bottom of the FOV. It corresponds to a strong $\boldsymbol{B}$-field region that persists and slowly evolves throughout the observation window. We designate it as the ROI and denote it by a green square in the four right panels. The ROI is not associated specifically with either upflows or downflows, as seen from the Dopplergram.

We also show the resulting distributions of the LOS and transverse magnetic field components in Figure 3. Negative polarity in the ROI is clearly seen in the skewed shape of the B_z histogram. As seen from the bottom left panel, other regions with strong polarization signals are much smaller in extent. They are also more transient, highlighting the difficulties of QS polarimetric observations.

As can be seen in Figure 1, the polarimetric signal, particularly in Q and U (panels (b) and (c)), is quite weak in our data (<200 G in most of the FOV). This is of course to be expected in the QS regime, where magnetic fields are only strong enough to produce distinct linear polarization features in 3%–16% of pixels in the FOV of SUNRISE/IMaX (Kianfar et al. 2018; Liu et al. 2022). In parts of the analysis that follows, we only consider regions of the FOV with signal strengths above a certain threshold. We choose the threshold of 50 G for masking out pixels with insufficiently strong magnetic fields, for the following reasons: (1) 50 G is approximately equal to 3σ in magnetic field strength distribution (bottom right panel of Figure 3), (2) the subset of pixels in the FOV with $B > 50$ G closely (within 5 G) corresponds to the pixels where at least one of the Q, U, and V spectra exhibits strong enough ($>3\sigma$) deviations from the continua, and (3) this threshold is consistent with the minimum horizontal field strength described in Kianfar et al. (2018), where the strength of linear polarization features in IMaX magnetograms was found to be in the range 50–500 G.

3.1.1. Azimuth Disambiguation

Azimuthal 180° ambiguity is a well-known problem wherein spectropolarimetric inversions based on the Zeeman effect produce two solutions for the $\boldsymbol{B}$-field azimuth, and the two solutions are mathematically equally valid. Several solutions to this problem have been proposed. These include global optimization mechanisms, such as ME0, where the preferred magnetic field configuration results in a globally minimized magnetic energy (Leka et al. 2009b). Other methods select the orientation of magnetic fields that results in the highest B_z if the magnetogram is taken off the disk center, or they look for opposite polarities and select an orientation that would close the field lines between the polarities (Metcalf et al. 2006). It should be noted that none of these methods have been rigorously tested in the QS regime, as linear polarization strength is usually too low to adequately employ these methods.

In this work, we attempt to use three (and end up using two) methods to disambiguate azimuths: ME0, randomization, and Poynting flux optimization. We first use ME0, as it is the most physically rigorous of the three methods and it has been extensively used, including in the Hinode and SDO/HMI data processing pipelines (Leka et al. 2009a; Hoeksema et al. 2014). ME0, or the minimum energy method, is an optimization algorithm that minimizes the global quantity $\lambda|J_z| + |\nabla \cdot \boldsymbol{B}|$, where J_z is the vertical current and λ is a modifiable scalar parameter that determines the relative importance of the two terms. As mentioned, ME0 has not been tested on QS data, so, to that end, we test it on synthetic magnetograms obtained from the 3D MHD STAGGER code (see Section 2.2). Unfortunately, ME0 performs poorly on the QS magnetograms produced by STAGGER, likely due to the different physical assumptions under which STAGGER and ME0 operate. The

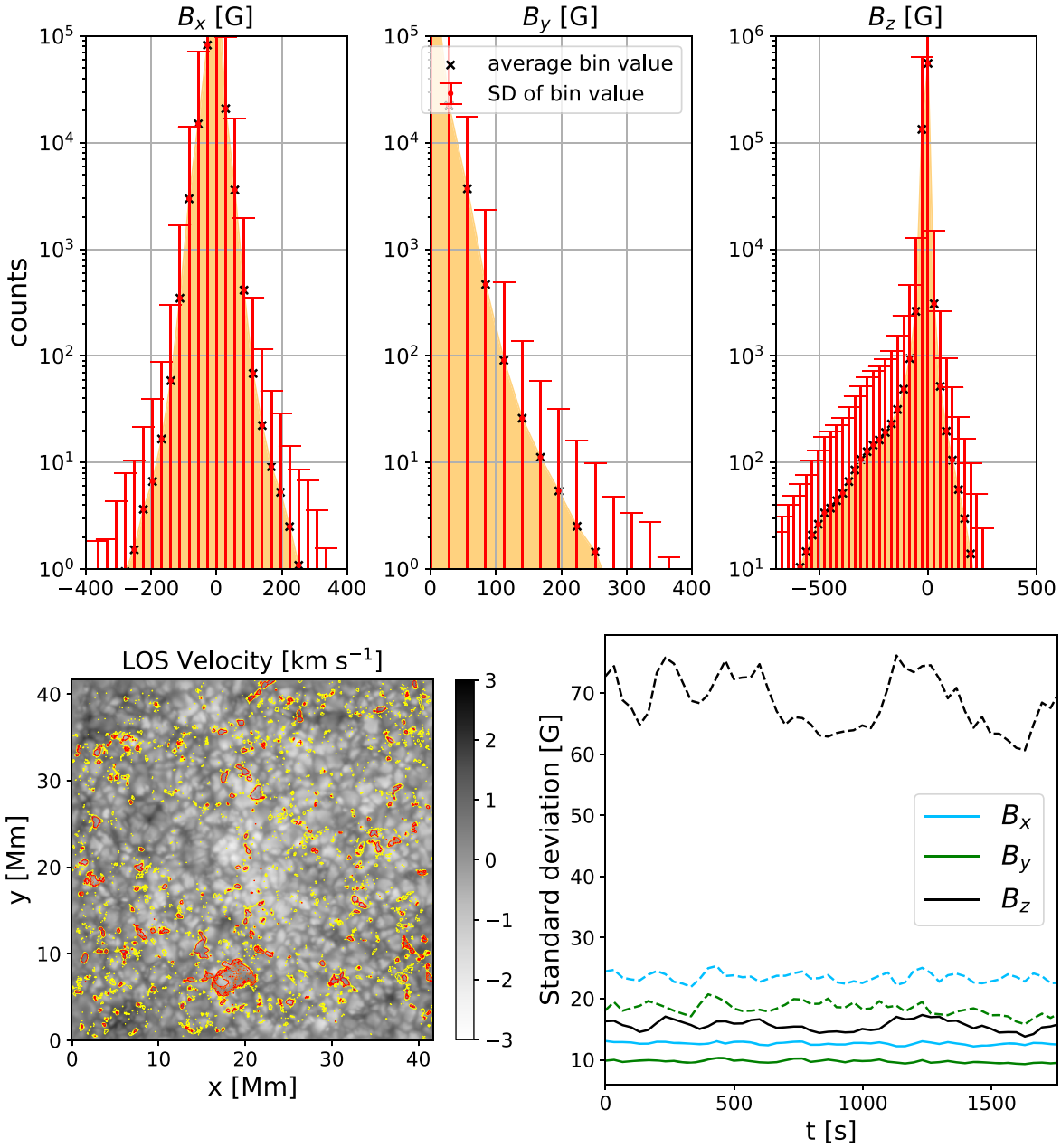

Figure 3. Distributions of $\boldsymbol{B}$-field components in IMaX magnetograms obtained with Milne–Eddington inversions, before disambiguation at $t = 1430$ s. Top row: histograms of $\boldsymbol{B}$-field components, showing the average and standard deviation in each bin taken over all magnetograms during the observation window. Relatively strong negative polarity is evident in the nonsymmetric B_z histogram. Bottom row, left: LOS velocity map with overlaid contours corresponding to area where the polarimetric signal exceeds 3σ (yellow) and 5σ (red) at $t = 1430$ s. Bottom row, right: standard deviation in $\boldsymbol{B}$-field components as a function of time taken over the entire FOV (solid lines) and only over pixels with a polarimetric signal (at least one of the Stokes Q, U, and V vectors) in excess of 3σ from the continuum (dashed lines). The B_y variance is the lowest, since these magnetograms have not been solved for the 180° ambiguity. For the same reason, the B_y histogram in the top row does not include negative values. For more discussion on azimuthal ambiguity, see Section 3.1.1.

issue with ME0 validation warrants a more detailed investigation, but we leave it for future work, as it is not the focus of the present paper.

While we cannot use full ME0 capabilities, the code is capable of performing potential-field acute-angle disambiguation. We use this method to disambiguate azimuths in the first frame, and for each subsequent frame, we resolve the ambiguity using an acute angle with respect to the previous frame. Another approach is to use the regular ME0 disambiguation while setting the λ weighting factor for $|J_z|$ to 0. The minimized quantity is then simply the divergence of the magnetic field. As in the potential-field disambiguation, we only apply this method to the first frame and then select the azimuths resulting in an acute angle with respect to the previous frame. In both cases this is done in order to minimize temporal discontinuities. While not strictly physical, this approach has been taken before, e.g., in Kaithakkal et al. (2023).

In the absence of a validated physical disambiguation method, we ask two questions: How sensitive is Poynting flux to the orientation of transverse magnetic fields (in other words, how much does the "choice" of azimuth affect our computed

quantities of Poynting flux), and what is the maximum Poynting flux that can be obtained from any given magnetogram that is yet to be disambiguated? These two questions lead us, respectively, to two other disambiguation methods: azimuth randomization and Poynting flux optimization.

Azimuth randomization can be thought of as an absolutely imperfect disambiguation, wherein we randomly add either 0° or 180° to the azimuth value of each pixel in a magnetogram. The random assignment of each pixel is performed independently of its neighboring pixels or earlier azimuth values in that pixel. Thus, this method yields a disambiguated magnetogram that almost certainly has spatial and temporal discontinuities in transverse field orientations.

The Poynting flux optimization disambiguation method consists of two steps: In the first magnetogram ($t = 0$), we disambiguate azimuths in each pixel by selecting the one that results in the higher value of S_z as computed using the ideal MHD method, i.e., using Equation (3). Then, for each consecutive magnetogram, we select for each pixel the azimuth value that is closer to the azimuth value of that pixel in the previous frame. In contrast with the randomization method, where every pixel is completely independent of both its surrounding pixels and its iteration in adjacent magnetograms in the time series, the Poynting flux optimization method results in some degree of spatial and temporal azimuth continuity, while also providing us a physical ceiling (i.e., upper boundary) for the Poynting flux. We stress, however, that this disambiguation method is only physically meaningful insofar as it provides the ceiling for Poynting flux. The outputs of the disambiguation methods used in this work are shown in Figure 4.

3.2. Electric Field Inversion Methods

To find the electric field needed to estimate the Poynting flux (Equation (1)), we use two approaches. The first "ideal MHD" approach strictly enforces the ideal MHD condition (Equation (3)). We then use Doppler measurements to derive the vertical velocity component and two reconstruction methods, FLCT and DeepVel, to invert the transverse velocity component (see Section 3.2.1 below). In the second "inductive" approach we use the PDFI_SS method to derive the electric field directly by inverting Faraday's law without necessarily enforcing the ideal MHD condition (see Section 3.2.2 below).

3.2.1. Transverse Velocity Inversion Methods

As shown in Section 3, the full plasma velocity vector (or alternatively, the horizontal electric field) is required to compute Poynting flux. Unlike the LOS velocity, which could be recovered from Doppler data (e.g., Welsch et al. 2013), transverse velocities cannot be directly inferred from observables. The two velocity retrieval methods we use in this work are FLCT (Fisher & Welsch 2008) and a convolutional neural network, DeepVel (Asensio Ramos et al. 2017).

FLCT (Welsch et al. 2007) is a plasma flow tracking method that takes two consecutive magnetograms or intensitygrams and, using a finite sliding window, infers the plane-of-sky displacement needed to produce the second map from the first one. It has been used as the flow inversion method for PDFI_SS (Kazachenko et al. 2015; Lumme et al. 2019; Afanasyev et al. 2021) and for tracking flows in various environments (e.g., Löptien et al. 2016; Tremblay et al. 2018), but it has some constraints. The main constraint of the FLCT approach is that it assumes that any change in continuum or

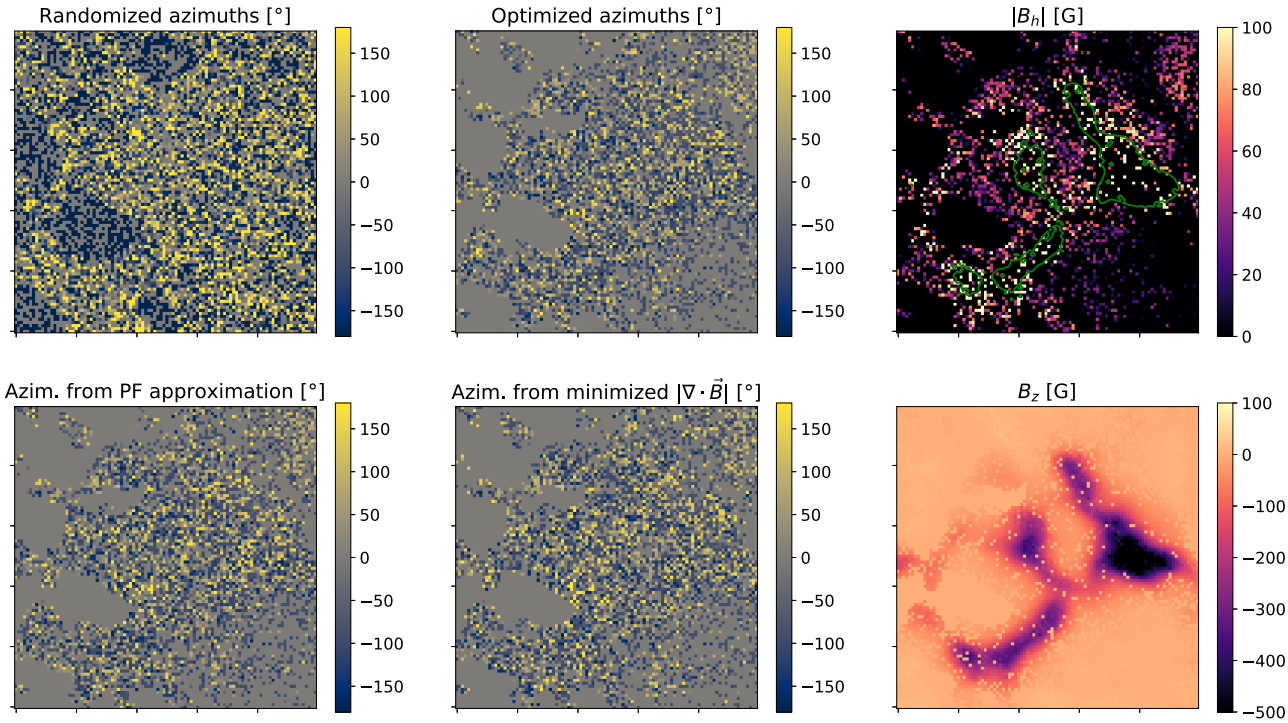

Figure 4. Close-up view of the strong magnetic field ROI at the bottom of the FOV (see panels (e)–(h) of Figure 1) showing the magnetic field azimuthal angles obtained via randomization (top left), optimization (top center), matching to the potential field (bottom left), and minimizing $\boldsymbol{B}$-field divergence (bottom center). The top right panel shows the spatial distribution of the horizontal magnetic field in the same region, where the green contours correspond to regions with $|\boldsymbol{B}| > 200$ G. The bottom right panel shows the LOS magnetic field.

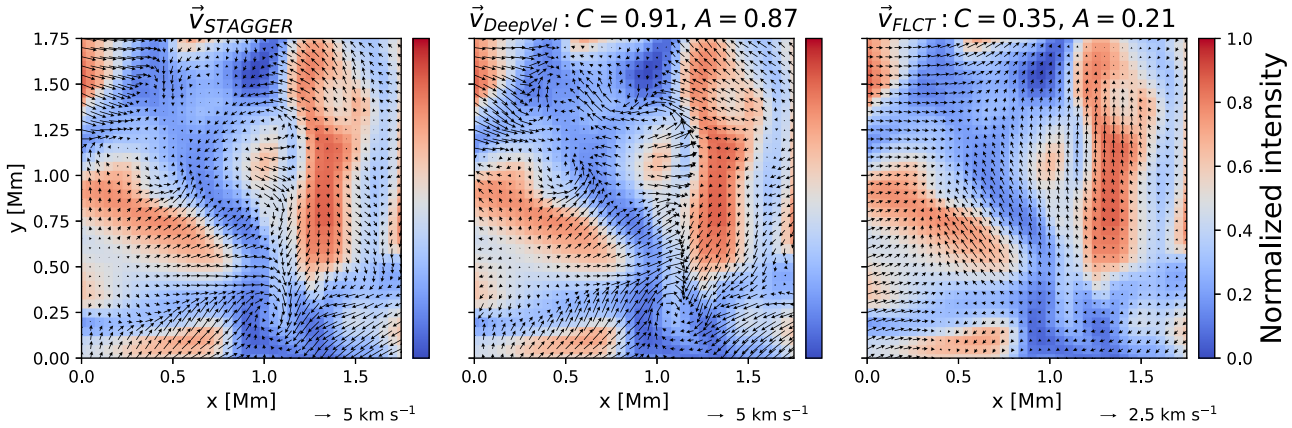

Figure 5. Comparison between the velocity fields computed by the STAGGER simulation (left; reference) and those predicted by the DeepVel (center) and FLCT (right) velocity tracking methods. Both the FLCT and DeepVel velocity fields are obtained using STAGGER-simulated QS intensities, which serve as a background for the figure. Note the different scale for the FLCT vector arrows.

magnetic field intensity is due to advective motion without obeying the induction equation (i.e., FLCT measures an optical flow). Second, FLCT has been applied either to data with relatively strong magnetic fields (Welsch et al. 2012; Lumme et al. 2019), where tracking is made possible by relatively high S/N, or to low-resolution and large-FOV images, where the objective is to track meso- and supergranular motions (Fisher & Welsch 2008). Neither of these contexts applies to our QS case: magnetic concentrations are, for the most part, transient and limited in spatial extent and strength, making it necessary to rely on continuum images, and the relevant scales of plasma motions are well below even mesogranular scales.

To validate FLCT plasma flow inferences in a setting more closely resembling that of the IMaX observations, we apply FLCT to continuum images from STAGGER simulations. We find the correlation between the FLCT and reference flows is low, with a Pearson correlation coefficient of $r < 0.45$. The correlation is even weaker if the σ parameter, which defines the width of the sliding Gaussian window, is lower than 10 pixels or higher than 15. In our work, we pick $\sigma = 10$, as it produces the strongest correlation. Following the analyses in Schrijver et al. (2006) and Tremblay et al. (2021), we consider three other correlation metrics between the reference STAGGER velocities and the velocities obtained from inversions: the spatially averaged relative error

$$E_{\rm rel}[\boldsymbol{v}_{\rm inv}, \boldsymbol{v}_{\rm ref}] \equiv \left\langle \sqrt{\frac{(\boldsymbol{v}_{\rm ref} - \boldsymbol{v}_{\rm inv}) \cdot (\boldsymbol{v}_{\rm ref} - \boldsymbol{v}_{\rm inv})}{\boldsymbol{v}_{\rm ref} \cdot \boldsymbol{v}_{\rm ref}}} \right\rangle,$$

the vector correlation coefficient

$$C[\boldsymbol{v}_{\rm inv}, \boldsymbol{v}_{\rm ref}] \equiv \frac{\langle \boldsymbol{v}_{\rm inv} \cdot \boldsymbol{v}_{\rm ref} \rangle}{\sqrt{\langle \boldsymbol{v}_{\rm ref} \cdot \boldsymbol{v}_{\rm ref} \rangle \cdot \langle \boldsymbol{v}_{\rm inv} \cdot \boldsymbol{v}_{\rm inv} \rangle}},$$

and the cosine similarity index, which measures the global spatial distribution of velocity vector orientations:

$$A[\boldsymbol{v}_{\rm inv}, \boldsymbol{v}_{\rm ref}] \equiv \left\langle \frac{\boldsymbol{v}_{\rm inv} \cdot \boldsymbol{v}_{\rm ref}}{\|\boldsymbol{v}_{\rm inv}\| \|\boldsymbol{v}_{\rm ref}\|} \right\rangle,$$

where the $\langle \cdot \rangle$ operation denotes spatial averaging. The C coefficient is defined so that it is 0 when the velocity vectors are perpendicular everywhere and 1 when they are parallel everywhere. Likewise, the A coefficient is -1 when the vectors are antiparallel and 1 when they are identical. Thus, the agreement between two vectors is the better the closer both C and A are to unity. For the mathematical expressions of these metrics, see Equations (3)–(5) in Tremblay et al. (2021). For FLCT, the values of these metrics are ($E_{\rm rel} = 1.09$, $C = 0.35$, $A = 0.21$). The FLCT and reference STAGGER flows are also qualitatively different (see Figure 5, left and right panels). The STAGGER velocities show a clear pattern of divergence in granules and convergent flows with vortices in intergranular lanes (IGLs), whereas the FLCT velocity fields are much more laminar (and smaller in magnitude) on average.

We find that FLCT velocity inferences in the QS can be improved by averaging instantaneous velocities over 30 minute time windows (Asensio Ramos et al. 2017; Tremblay et al. 2018). The correlation coefficient between the FLCT and STAGGER velocities then improves to $r = 0.75$, but considering the photospheric timescales are on the order of 5 minutes, such improvement comes at a cost of losing time-dependent information. We therefore conclude that the FLCT method is an inadequate velocity inversion method for our purposes, where instantaneous or near-instantaneous (<2.5 minute) velocities are to have high fidelity.

In addition to FLCT, we use DeepVel—a convolutional neural network that has been previously used to infer velocities on granular scales, including in the QS (Asensio Ramos et al. 2017; Tremblay et al. 2018; Tremblay & Attie 2020). DeepVel is trained using simulation data, for which all flow components are known, to map a pair of input images (e.g., continuum intensity images at two time steps) to the transverse flows at a given optical depth or geometrical height. This approach is known as supervised learning. In other words, the output velocities approximate what the flows in the training simulation would be if we assume that the input data provided to the neural network was generated by the training simulation (i.e., there is a model dependency). For this work, we train DeepVel on a set of STAGGER data frames. To test the trained network, we run it on a STAGGER intensity map outside of the training set. The test map has the same properties described in Section 2.2. As in previous works, we find that the DeepVel instantaneous velocities are highly ($r = 0.91$) correlated with the simulated velocities (Figure 5).

We find that the correlation metrics' values are significantly higher for DeepVel ($E_{\rm rel} = 0.74$, $C = 0.91$, $A = 0.87$) than for

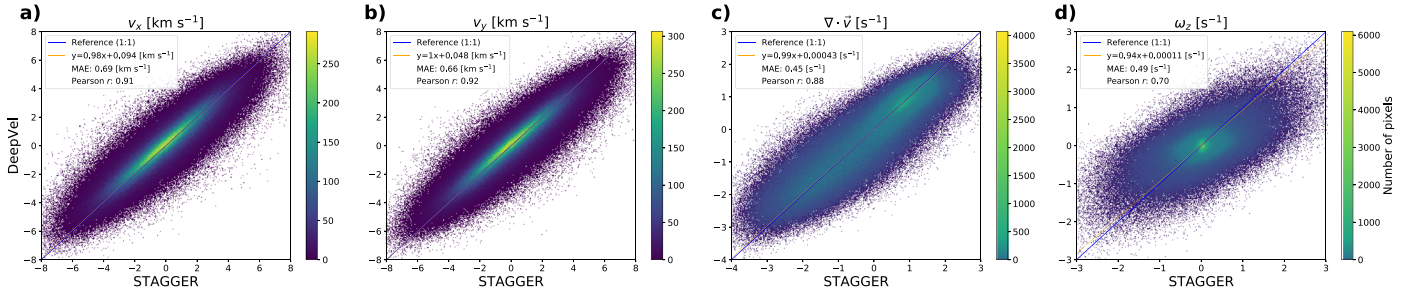

Figure 6. Scatterplots comparing the velocities inferred by the DeepVel neural network to the STAGGER simulation (reference) velocities: (a) v_x, (b) v_y, (c) $\nabla_h \cdot \boldsymbol{v}_h$, and (d) $\omega_z = [\nabla \times \boldsymbol{v}]_z$. Statistical metrics are provided in the legend to each panel. MAE stands for mean absolute error.

FLCT. These are stark improvements over FLCT in terms of the accuracy achieved without losing temporal resolution via time averaging. Even though DeepVel is limited in ways that may have implications for our results (as discussed further in Section 5 and, e.g., in Tremblay & Attie 2020), we choose to apply DeepVel to IMaX intensitygrams to retrieve transverse velocities in our analysis. Hereafter, all retrieved transverse velocities are obtained with DeepVel rather than with FLCT. We note, however, that DeepVel is not without its limitations. Even though we get really good agreement ($r \approx 0.9$) between simulation and DeepVel velocities and divergences, DeepVel is not as reliable at reproducing vorticities (see Figure 6, panel (d)).

3.2.2. PDFI Electric Field Inversion Method

To find Poynting flux without assuming ideal MHD conditions, we use the PDFI_SS method (Fisher et al. 2020). Briefly, the magnetic field in the PDFI_SS method is expressed as a sum of poloidal and toroidal components. This decomposition allows us to derive the *inductive* component of the electric field from observed quantities by uncurling Faraday's law (Equation (2)). The gradient of the scalar part of the electric field that appears due to the uncurling of Faraday's law is called the "noninductive" component and could be computed from additional constraints, including the ideal MHD constraint $\boldsymbol{E} \cdot \boldsymbol{B} = 0$ (Kazachenko et al. 2014).

PDFI_SS has been used to describe the evolution of Poynting flux and magnetic helicity in multiple works, but notably, these were all concerned with either observed or simulated active regions (e.g., Kazachenko et al. 2015; Lumme et al. 2019) or regions of flux emergence (e.g., Afanasyev et al. 2021). To our knowledge, PDFI_SS has not been applied to QS magnetic fields. Apart from the general challenge of studying QS magnetism, the reliance of PDFI_SS on the $\frac{\partial \boldsymbol{B}}{\partial t}$ term in Faraday's law makes it especially susceptible to noise. To mitigate the influence of noise, we set the `bmin` parameter, which masks pixels with lower magnetic field strength (see Section 10.2 in Fisher et al. 2020), to 50 G—the same threshold we choose in Section 3.1. PDFI_SS also requires high-cadence observations, so as to not miss the transient magnetic concentrations that are ubiquitous in the QS (Gošić et al. 2018).

4. Results

We compute Poynting fluxes using two approaches: from velocity fields together with the ideal MHD assumption, and from PDFI_SS electric fields, where time derivatives of magnetic fields are used as a source term. Within each approach, we use randomly disambiguated azimuths and

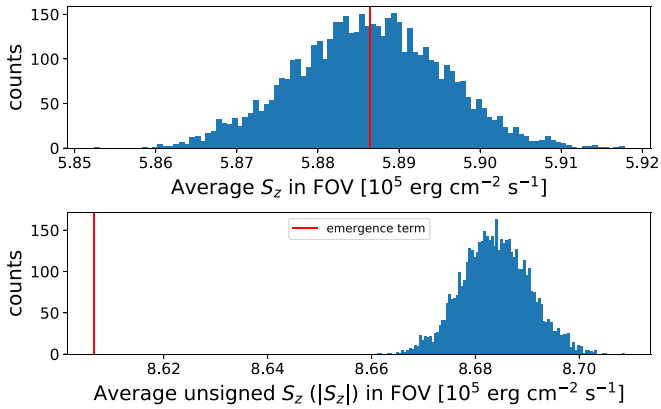

Figure 7. Histograms of the spatially averaged Poynting flux within the FOV at $t = 1430$ s. The computations are performed using the ideal MHD method with 5000 realizations of randomized azimuth disambiguation. The vertical red line corresponds to the value of the emergence term of S_z (see Section 4).

azimuths obtained via the optimization procedure (see Section 3.1.1). We show the temporal evolution of Poynting fluxes in both settings in Figure 8.

As discussed in Section 3.1.1, the azimuthal orientation of vector magnetic fields can affect Poynting flux magnitudes. Since one of our two principal methods of azimuthal disambiguation relies on randomizing azimuths on a pixel-by-pixel basis, we investigate the resulting uncertainty in Poynting fluxes in the ideal MHD setting by repeating the randomization for each magnetogram 5000 times. We find the average Poynting flux estimates in each frame to be highly robust to different realizations of azimuth randomization, with both signed (net) and unsigned (absolute value) fluxes tightly clustered (see Figure 7). We also find that in the ideal MHD setting, the emergence term $v_z B_h^2$ dominates both the signed and unsigned fluxes over the shear, or wave, term $(\boldsymbol{v}_h \cdot \boldsymbol{B}_h)B_z$ (see Equation (4)), which accounts for less than 1% of the total vertical Poynting flux.

The left panel of Figure 8 shows the Poynting flux evolution for the ideal MHD case. The different plot colors correspond to the spatially averaged Poynting flux ($\overline{S_z}$) in all pixels as well as only in pixels where the magnetic field strength ($|\boldsymbol{B}|$) exceeds 50 G and 100 G thresholds. The first thing to note here is that the choice of azimuth disambiguation method plays a negligible role in the S_z values. The largest difference is in the first frame, where, in the optimization procedure, we explicitly optimize for the largest S_z value. In just over 1 minute this difference disappears, and the $\overline{S_z}$ values stabilize within the range $6.0 \pm 0.56 \times 10^5$ erg cm^{-2} s^{-1} and $1.1 \pm 0.087 \times 10^7$ erg cm^{-2} s^{-1} for all pixels and for pixels with high $\boldsymbol{B}$-fields, respectively. This is consistent with our analysis of the

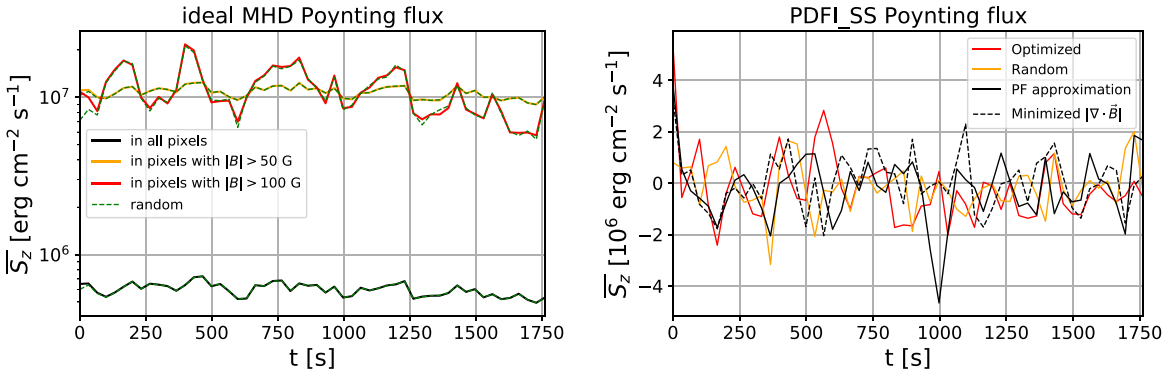

Figure 8. Left panel: temporal evolution of the average Poynting flux, computed using the ideal MHD assumption and DeepVel velocities. The dashed green lines represent Poynting flux computed in the same sets of pixels as the solid lines, but using random azimuths instead of azimuths obtained via the Poynting flux optimization procedure. Right panel: Poynting flux computed via PDFI_SS and DeepVel velocities and averaged over pixels above the threshold $\boldsymbol{B}$-field value (see Section 3.2.2), using random azimuths (orange line), optimized azimuths (red line), and azimuths obtained from the potential-field acute-angle method (solid black line) and from imposing $|\nabla \cdot \boldsymbol{B} = 0|$ (dashed black line). Note the different y-axis limits.

randomization procedure shown in Figure 4, where we find very little variation in the FOV-integrated S_z across different azimuth realizations.

We also observe that selecting pixels with relatively strong $|\boldsymbol{B}|$ increases the average S_z by an order of magnitude, but there is not much variation between a 50 G and a 100 G threshold (or even a 150 G threshold and above, which are not shown here). Increasing the threshold to 100 G, however, reveals quasiperiodic oscillations that could conceivably be linked to 5 minute photospheric oscillations (Leighton et al. 1962; Ulrich 1970).

Figure 8 (right panel) shows Poynting fluxes derived from the PDFI_SS method. Recall that, since we set the `bmin` parameter to 50 G, all pixels with magnetic fields below that threshold are set to zero and are not considered in the following analysis. We find that these estimates are very different from the ideal MHD estimates shown on the left panel. First, the optimized (randomized) $\bar{S}_z$ is $-2.1 \pm 13 \times 10^5$ ($-1.3 \pm 9.4 \times 10^5$) erg cm^{-2} s^{-1}—significantly lower, even in terms of absolute values, than the $\bar{S}_z$ in the ideal MHD case with pixels with weak magnetic fields counted. Second, in both cases (randomized and optimized azimuths), S_z oscillates around zero and is sometimes well below it, meaning that magnetic energy is transported downward instead of upward. Third and less surprisingly, the S_z values obtained from the randomization and S_z optimization disambiguation methods are much more different from each other than they are in the ideal MHD case. This is due to the fact that PDFI_SS uses spatial and temporal derivatives of the $\boldsymbol{B}$-fields to compute S_z, and both are affected in the randomization procedure, which produces highly discontinuous magnetic field configurations, more so than in the case of optimized azimuths. However, the two other azimuthal ambiguity resolutions—from the potential field and from $|\nabla \cdot \boldsymbol{B}| = 0$—also produce Poynting fluxes that oscillate frequently around zero and almost never exceed 2×10^6 erg cm^{-2} s^{-1}. This most likely indicates that significant spatial and temporal discontinuities are present in IMaX QS magnetograms regardless of the azimuthal disambiguation method, as can be seen in Figure 4.

To evaluate how Poynting flux and its components vary in height, we use the outputs of MURaM simulations, since the IMaX data set only includes data from one optical surface. In Figure 9, we compare Poynting fluxes derived directly from MURaM simulations. We find that the MURaM averaged

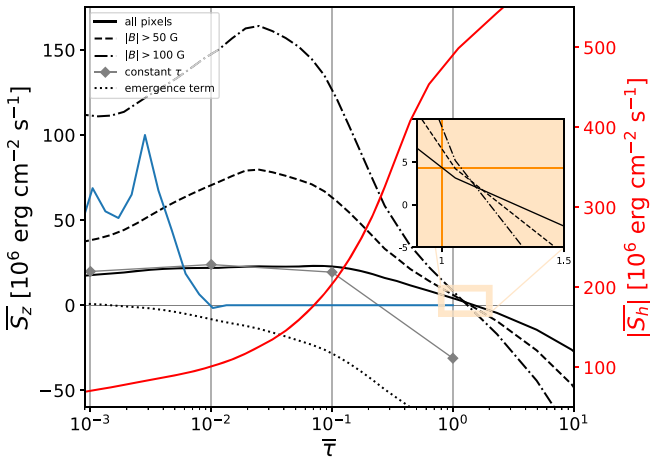

Figure 9. Average Poynting flux in MURaM simulations as a function of optical depth. The red curve shows the transverse Poynting flux. The x-axis corresponds to a vertical range of ∼0.35 Mm. The black curves (gray diamonds) correspond to vertical Poynting flux computed on geometrical (optical) surfaces and spatially averaged over subsets of pixels with varying magnetic field strengths. The dotted curve represents the emergence term ($\nu_z B_h^2$) of the vertical Poynting flux averaged over all pixels on geometrical surfaces. The blue curve represents the response function of the Fe I 5250.2 Å line in IGLs in arbitrary units. Its peak is at $\bar{\tau} = 3 \times 10^{-3}$, which is slightly below 400 km. The horizontal and vertical orange lines in the inset represent $S_{z,\mathrm{thr}}$ from Withbroe & Noyes (1977; see Section 5) and the $\bar{\tau} = 1$ surface, respectively.

vertical Poynting flux reverses signs very close to the $\tau = 1$ surface, and that it is exceeded by $|S_h|$ from the convection zone until well above $\tau = 0.1$. We find that at $\bar{\tau} = 1$, $\overline{S_z} = 4.38 \times 10^6$ erg cm^{-2} s^{-1}, and it rises to 2.28×10^7 erg cm^{-2} s^{-1} at $\bar{\tau} = 0.1$.

5. Discussion

In their seminal paper, Withbroe & Noyes (1977) derived a threshold of upward energy flux from the photosphere that would be necessary to explain chromospheric and coronal heating in the QS: $S_{z,\mathrm{thr}} = 4.3 \times 10^6$ erg cm^{-2} s^{-1}. In the MURaM simulations, the vertical Poynting flux at $\bar{\tau} = 1$ is just above the $S_{z,\mathrm{thr}}$ value from Withbroe & Noyes (1977). This is consistent with existing MURaM simulations, where the hot corona is maintained by photospheric magnetoconvection (Rempel 2017; Breu et al. 2022, 2023). However, we find

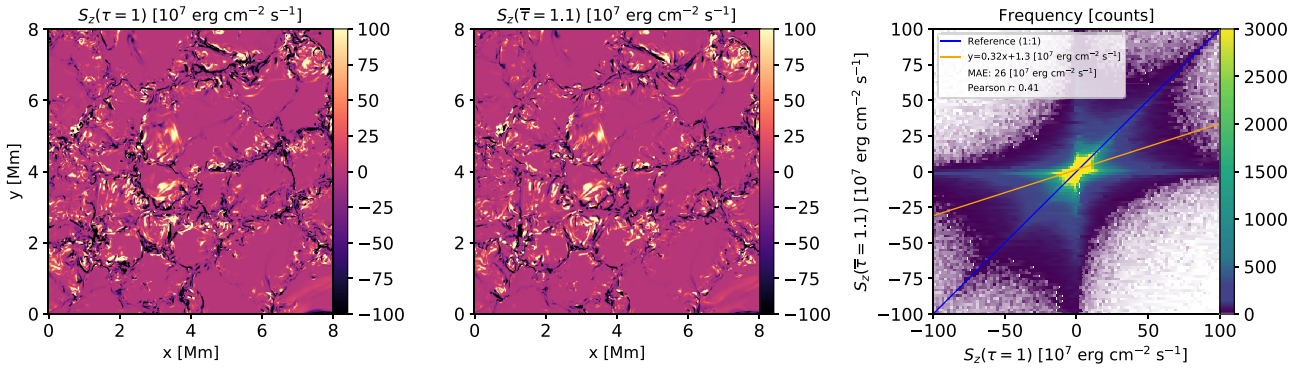

Figure 10. Vertical Poynting flux computed on optical surface $\tau = 1$ (left panel) and geometrical surface $z = 0$ Mm, where the spatially averaged optical depth is $\overline{\tau} = 1.1$ (center panel). Notice the concentration of both positive and negative S_z in the IGLs. On the right panel is a 2D histogram comparing pixel-by-pixel S_z values computed on optical and geometrical surfaces. Note the different scales for the axes.

that in IMaX observations, there is not enough Poynting flux whether we use the ideal MHD method or PDFI_SS, unless we consider only strong $\boldsymbol{B}$-field pixels in the ideal MHD case (Figure 8). Furthermore, in the ideal MHD case, vertical Poynting flux is lower than the minimum value required for heating by an order of magnitude. On the other hand, PDFI_SS values are closer to 4.3×10^6 erg cm^{-2} s^{-1} in magnitude, but are frequently negative, indicating downward energy flux.

What are the possible causes of discrepancies between different Poynting flux estimates, and why is Poynting flux negative in some of them? We propose several physical and methodological explanations.

A nontrivial methodological issue with our analysis is the weak signal in the QS. This is particularly severe when it comes to the Q and U Stokes vector signal strength, which adversely affects our inversions of $\boldsymbol{B}_h$. Even in the ROI, where magnetic field strength exceeds 200 G—a relatively high value for our data set—there are significant discontinuities in the spatial distribution of the horizontal magnetic field (right panel of Figure 4). These gaps affect both the ideal MHD and PDFI_SS Poynting flux inversion methods. In ideal MHD, as can be seen from Equation (4), Poynting flux is highly sensitive to $\boldsymbol{B}_h$ as it appears in both terms of the expression. In PDFI_SS, $\boldsymbol{B}_h$ uncertainties affect both the $\boldsymbol{v} \times \boldsymbol{B}$ term as above and the spatial and temporal derivatives of the magnetic field.

Uncertainties in transverse magnetic field inversions B_h propagate into issues with azimuth disambiguation. However, we see that with the IMaX signal strength, they do not meaningfully affect Poynting flux estimates, especially in the ideal MHD scenario (Figure 7). Instead, the emergence term $v_z B_h^2$ is responsible for virtually all signed Poynting flux and 99% of unsigned Poynting flux. This is qualitatively consistent with some of the existing literature (e.g., Liu & Schuck 2012), but this fraction is much higher than in previous works. This is likely due to the weak magnetic field signal in our observational sample: for the shear term to be present, both linear and circular polarization signatures must be strong in the same pixel.

Transverse velocity inversions are another potential source of errors in Poynting flux inversions, though in the present work they are also likely to be secondary-order errors. As discussed in Section 3.2.1, vorticity values inferred with DeepVel may be unreliable (Figure 6). Further, we do not have access to "ground truth" when it comes to transverse velocity on the real Sun, and a neural network trained using supervised learning generates predictions that are only as good as the simulations they were trained on (from the relationship between continuum intensity and transverse flows, to the topology and magnitude of the flows). In MHD simulations, including STAGGER and MURaM, vortices are mostly concentrated in IGLs and they have been shown to be spatially correlated with vertical Poynting flux in MURaM simulations (Yadav et al. 2020, 2021). This, then, presents a clear avenue for improvement, particularly when DKIST observations with higher spatial resolution (down to 0.″03; Rimmele et al. 2020) become available, since features in IGLs are especially vulnerable to resolution effects. Another way to improve the neural network approach is to train it to match coherence spectra, i.e., to match velocities at different frequencies in the Fourier space, as was done in Ishikawa et al. (2022).

Poynting flux inversions themselves can still be improved. We have already explained how, unlike PDFI_SS, the ideal MHD method does not account for Poynting flux derived from $\frac{\partial \boldsymbol{B}}{\partial t}$, but PDFI_SS also has limitations. It has not been tested in the QS regime, particularly when only one polarity (negative in our case) of B_z is present in the FOV.

Another explanation for negative vertical Poynting flux could be physical factors. There are several pieces of evidence in favor of that possibility.

First, we are studying Poynting flux at the boundary layer between convection-dominated layers below the photosphere and the radiation-dominated atmosphere. In such an environment, it is reasonable to expect all energy fluxes (e.g., mass flux, convective flux) averaged over a representative FOV to become dominated by their horizontal components, which are mostly self-canceling, while vertical components approach near-zero values (Steiner et al. 2008). This is indeed the case in IMaX observations. Assuming ideal MHD conditions, we find that the horizontal Poynting flux ($|S_h|$) exceeds $|S_z|$ by a factor of $\approx$3. Silva et al. (2022) analyzed the same IMaX data set we use in our work and reported an even higher ratio of horizontal to vertical Poynting fluxes, likely due to the higher velocity values in their inversions.

In the MURaM simulations, we see that Poynting fluxes are principally concentrated in IGLs. An important corollary from this observation is that the emergence term of Poynting flux, which can only be negative provided $v_z < 0$, is primarily negative in photospheric and chromospheric heights, which is indeed what we find (see Figure 9). Therefore, on average, the wave term of Poynting flux is larger in magnitude than the emergence term, in stark contrast with our findings in the IMaX

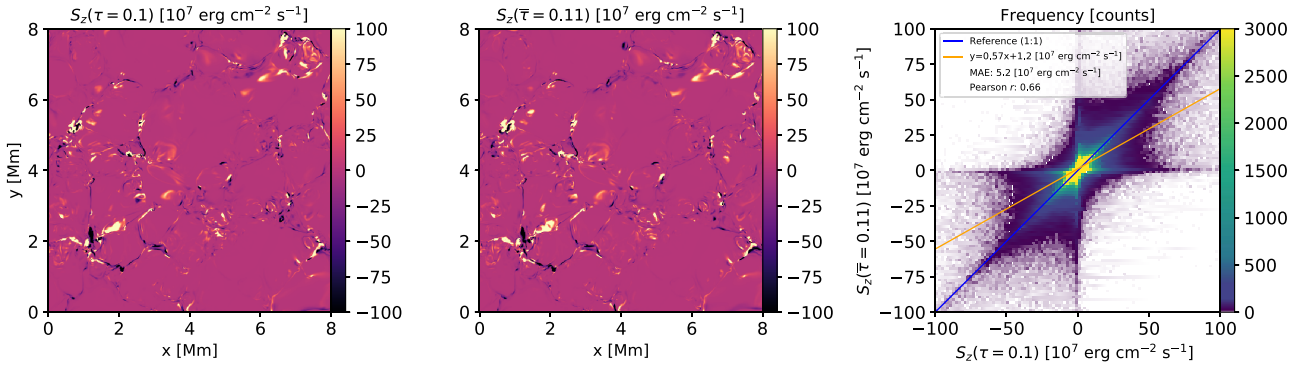

Figure 11. Same as Figure 10, but for the optical depth $\tau = 0.1$ and geometrical surface $z = 0.128$ Mm with spatially averaged optical depth $\overline{\tau} = 0.11$.

Table 1
Summary of Photospheric Poynting Flux Estimates in the Present Work and in Existing Literature

Method	Target	$\overline{S_z}$ (erg cm^{-2} s^{-1})
Present work, ideal MHD	observed QS, all pixels	$6.0 \pm 0.56 \times 10^5$
Present work, ideal MHD	observed QS, high $\boldsymbol{B}$-field pixels	$1.1 \pm 0.087 \times 10^7$
Present work, PDFI_SS	observed QS	$-0.21 \pm 1.3 \times 10^6$
Present work, MURaM	simulated QS, geometrical surface $z = 0.000$ Mm ($\overline{\tau} = 1.1$)	4.36×10^6
Present work, MURaM	simulated QS, geometrical surface $z = 0.128$ Mm ($\overline{\tau} = 0.11$)	2.28×10^7
Present work, MURaM	simulated QS, optical surface $\tau = 1.0$	-3.11×10^7
Present work, MURaM	simulated QS, optical surface $\tau = 0.1$	1.94×10^7
Kazachenko et al. (2015), PDFI_SS	AR 11158	10^8–10^9
Welsch & Fisher (2016), ideal MHD	AR 10930, plage	$\approx 5 \times 10^7$

observations. As discussed above, this is likely due to a strong observational bias, wherein both the IGL structure and magnetic concentrations that are not trivially oriented (neither completely parallel nor perpendicular to the LOS) are subject to instrumental limitations. The observed ideal MHD Poynting fluxes in IMaX, which are dominated by the emergence term yet are positive, likely arise from magnetic concentrations located in granule interiors, such as those inside the ROI (see Figure 4). Analogs of such a structure can be seen in the MURaM simulations as well, e.g., in Figures 2 and 10 at $[x, y] = [3.5\,\text{Mm}, 3.5\,\text{Mm}]$ (just left of and below the center of the FOV).

There are of course caveats when it comes to optical depth. First, it is unclear what optical depth corresponds to the formation of the Fe I 5250.2 Å line, which we use for the spectropolarimetric inversions. It is evident that the line forms somewhere in the photosphere, but we are not aware of existing studies that looked at its response function. We find that this could be important, since in MURaM simulations average Poynting flux values are sensitive to changes in optical depth: from $\overline{\tau} = 1.1$ to $\overline{\tau} = 0.63$, $\overline{S_z}$ increases by a factor of 2.7 (see Figure 9). To see where the Fe I 5250.2 line could form, we calculate its response function using a MURaM atmospheric profile (Rempel 2014). We use one profile from granules and one from IGLs, and in both cases (the latter is shown in Figure 9) we find that the line forms in the photosphere (300–400 km), but that it has a broad formation height range.

The second caveat related to optical depth is that a constant-τ surface is very different from a constant-height surface, and Poynting fluxes computed on optical surfaces deviate significantly from those computed on geometrical surfaces with comparable optical depths averaged over the FOV (see Figures 10 and 11). In particular, while the average Poynting flux computed on the geometrical surface with $\overline{\tau} = 1$ may be sufficient to match energy losses in the chromosphere and corona, the average Poynting flux computed on the geometrical surface $\tau = 1$ is far from being sufficient, as it is -3.11×10^7 erg cm^{-2} s^{-1} (Figure 9). Despite these differences, we treat all of our vector quantities' components as being either parallel or perpendicular to the plane of the sky (and to the LOS). This can lead to unphysical results, since we are essentially dealing with vector projections and not true vectors. It is especially so in regions where optical surfaces are least aligned with the geometrical ones, such as on the boundaries between granules and IGLs. Incidentally, this is where (1) the MURaM vertical Poynting flux is primarily concentrated, (2) transverse flows have the most shear and vorticity, and (3) resolution constraints have the greatest detrimental effect (Leka et al. 2022).

6. Conclusions

In this work we use two approaches—the ideal MHD and PDFI_SS methods—to compute the average photospheric Poynting fluxes from IMaX polarimetric observations. We test several methods for deriving intermediate quantities required for computing Poynting flux. Principally, such quantities include the magnetic field azimuth, transverse velocities, and electric fields. We also look at the outputs of the 3D radiative MHD code MURaM between $\tau = 10^9$ and $\tau = -5 \times 10^{-8}$ to glean insights from simulated photospheric data.

Our quantitative estimates of Poynting flux do not reveal a consistent picture with respect to whether photospheric Poynting flux is sufficient to explain chromospheric and coronal heating (Table 1). However, we can outline several important findings:

1. The ideal MHD approach yields ambiguous estimates of S_z, but this could be explained by the quality of available data. When considering only pixels with relatively high magnetic field values ($|B| > 50$ G), the resulting average Poynting flux suffices to explain chromospheric heating, but S_z averaged over all pixels does not (Figure 8). It is possible that, due to instrumental limitations, we miss many of the small and/or transient magnetic concentrations.
2. The 180° azimuthal ambiguity barely affects the estimates of the ideal MHD approach (Figure 7). This is because Poynting fluxes derived via the ideal MHD method are dominated by the emergence term $v_z B_h^2$. This could also explain the lack of Poynting flux when it is averaged over all pixels. The importance of the emergence term has been reported before, but it is likely exaggerated in our results, since pixels with both vertical and transverse magnetic fields (which are both necessary to produce the wave term $(\boldsymbol{v}_h \cdot \boldsymbol{B}_h)B_z$ of Poynting flux) are difficult to detect in QS magnetograms. Indeed, in MURaM simulations, the wave term is on average positive and larger in magnitude than the emergence term, which is concentrated in IGLs and, consequently, is negative on average. When more advanced observations are available, such that the bias against the wave term is diminished and resolving azimuthal ambiguity becomes relevant, we point to our Poynting flux optimization method as a way to disambiguate azimuths while meaningfully constraining S_z.
3. Poynting flux obtained with the PDFI_SS method is highly time-dependent, insufficient for chromospheric and coronal heating, and negative in many of the frames in our time series (Figure 8). It is also sensitive to azimuth disambiguation. The variability and sensitivity to magnetic field azimuthal orientation can be caused by the reliance of PDFI_SS on spatial and temporal derivatives, combined with the noisy data sample. The closeness of the flux to zero can be attributed to the photosphere being a boundary layer between the convection-dominated subsurface and the radiation-dominated lower atmosphere.
4. MURaM simulations also display vertical Poynting flux that flips signs around $\tau = 1$ and is dominated by (unsigned) horizontal Poynting flux, supporting the boundary layer explanation (Figure 9). S_z in MURaM simulations is frequently negative around the $\tau = 1$ surface, particularly in IGLs (see Figures 2 and 10). At the same time, the upward Poynting flux is more than sufficient to explain chromospheric and coronal heating. While it may look like Poynting flux is close to the heating threshold around $\tau = 1$ (Figure 9), this region is in the deep photosphere, where the sign of the Poynting flux flips, and is below the formation height of most observable spectral lines. It should be noted that MURaM simulations that extend into the corona (Rempel 2017) produce a self-maintained QS corona (about 1.5×10^6 K) with sufficient Poynting flux. However, those simulations have lower resolution and the Poynting flux comes more from the braiding of the QS network field, which is mostly absent in our simulation set. MURaM simulations of coronal loops also show that photospheric energy output is sufficient to maintain a hot corona (Breu et al. 2022, 2023).

The main question—whether the observed QS photosphere produces enough magnetic energy in the form of Poynting flux to heat the chromosphere and corona—remains open. There are, however, promising signs that this uncertainty will be cleared up in the future. DKIST observations, particularly with the Visible Broadband Imager, DL-NIRSP, and Visible Tunable Filter instruments, can be used to observe photospheric magnetic fields with unprecedented polarization sensitivity, resolution, and cadence (Rimmele et al. 2020). Repeating this analysis with DKIST data is one of the most obvious avenues for future work.

We can also improve our methodology moving forward, particularly as it pertains to transverse magnetic field inversions, including azimuth disambiguation, and transverse velocity inversions. For the former, a physics-based approach such as ME0 is preferable to the more stochastic or optimizing approaches used in this work. We can also use acute-angle disambiguation, provided we have QS observations sufficiently far from the disk center. We may also achieve higher fidelity in transverse magnetic field inversions by using an inversion scheme that solves for the magnetic filling factor (Leka et al. 2022). For transverse velocity inversions, modifying DeepVel so that it is trained to match vorticity as well as velocity can be useful, since Poynting flux is associated with shear flows and vortices in IGLs.

Finally, numerical MHD simulations present a convenient avenue for exploring relationships between time- and height-dependent upward flux of magnetic energy and different structures in the QS. This area has remained largely unexplored, due to a lack of observational counterparts with which to verify potential findings, but it is more relevant now, in the era of DKIST. For an investigation of Poynting flux that is more directly comparable to observations, observables such as Stokes vectors must be computed using forward models and then inverted. It should be noted that it is unclear whether such an approach will result in physical values, since inversions produce quantities on optical surfaces, where vector cross-products are not meaningful. However, an approach involving forward modeling can be used to assess model fidelity and, by extension, whether the model can be used to make useful Poynting flux predictions. Detailed and focused studies of numerical simulations are therefore necessary.

Acknowledgments

This work is supported by NASA FINESST award 20-HELIO20-0004. This material is based on work supported by the National Center for Atmospheric Research, which is a major facility sponsored by the National Science Foundation under Cooperative Agreement No. 1852977. The authors thank Anna Malanushenko for general comments on the paper and K. D. Leka for her valuable advice on azimuth disambiguation. The authors also thank the anonymous referee for useful suggestions, particularly in regard to azimuth disambiguation.

Facility: SUNRISE (IMaX).

Software: pyMilne (de la Cruz Rodríguez 2019), ME0 (Leka et al. 2009b), FLCT (Fisher & Welsch 2008), DeepVel (Asensio Ramos et al. 2017), PDFI_SS (Fisher et al. 2020), MURaM (Rempel 2014).

ORCID iDs

Dennis Tilipman https://orcid.org/0000-0001-9361-6629
Maria Kazachenko https://orcid.org/0000-0001-8975-7605
Benoit Tremblay https://orcid.org/0000-0002-5181-7913
Ivan Milić https://orcid.org/0000-0002-0189-5550
Valentin Martínez Pillet https://orcid.org/0000-0001-7764-6895
Matthias Rempel https://orcid.org/0000-0001-5850-3119

References

Afanasyev, A. N., Kazachenko, M. D., Fan, Y., Fisher, G. H., & Tremblay, B. 2021, ApJ, 919, 7
Asensio Ramos, A., & Díaz Baso, C. J. 2019, A&A, 626, A102
Asensio Ramos, A., Requerey, I. S., & Vitas, N. 2017, A&A, 604, A11
Breu, C., Peter, H., Cameron, R., et al. 2022, A&A, 658, A45
Breu, C., Peter, H., Cameron, R., et al. 2023, A&A, 669, C1
Cheung, M. C. M., & Isobe, H. 2014, LRSP, 11, 3
de la Cruz Rodríguez, J. 2019, A&A, 631, A153
Fisher, G. H., Kazachenko, M. D., Welsch, B. T., et al. 2020, ApJS, 248, 2
Fisher, G. H., & Welsch, B. T. 2008, in ASP Conf. Ser. 383, Subsurface and Atmospheric Influences on Solar Activity, ed. R. Howe, 373
Gošić, M., de la Cruz Rodríguez, J., De Pontieu, B., et al. 2018, ApJ, 857, 48
Hoeksema, J. T., Liu, Y., Hayashi, K., et al. 2014, SoPh, 289, 3483
Ishikawa, R. T., Nakata, M., Katsukawa, Y., Masada, Y., & Riethmüller, T. L. 2022, A&A, 658, A142
Jafarzadeh, S., Solanki, S. K., Lagg, A., et al. 2014, A&A, 569, A105
Kaithakkal, A. J., Borrero, J. M., Yabar, A. P., & de la Cruz Rodríguez, J. 2023, MNRAS, 521, 3882
Kazachenko, M. D., Fisher, G. H., & Welsch, B. T. 2014, ApJ, 795, 17
Kazachenko, M. D., Fisher, G. H., Welsch, B. T., Liu, Y., & Sun, X. 2015, ApJ, 811, 16
Kianfar, S., Jafarzadeh, S., Mirtorabi, M. T., & Riethmüller, T. L. 2018, SoPh, 293, 123
Leighton, R. B., Noyes, R. W., & Simon, G. W. 1962, ApJL, 135, 474
Leka, K. D., Barnes, G., & Crouch, A. 2009a, in ASP Conf. Ser. 415, The Second Hinode Science Meeting: Beyond Discovery-Toward Understanding, ed. B. Lites et al., 365
Leka, K. D., Barnes, G., Crouch, A. D., et al. 2009b, SoPh, 260, 83
Leka, K. D., Wagner, E. L., Griñón-Marín, A. B., Bommier, V., & Higgins, R. E. L. 2022, SoPh, 297, 121
Liu, Y., Jiang, C., Yuan, D., & Zuo, P. 2022, ApJ, 928, 107
Liu, Y., & Schuck, P. W. 2012, ApJ, 761, 105
Löptien, B., Birch, A. C., Duvall, T. L., Gizon, L., & Schou, J. 2016, A&A, 590, A130
Lumme, E., Kazachenko, M. D., Fisher, G. H., et al. 2019, SoPh, 294, 84
Magic, Z., Collet, R., Asplund, M., et al. 2013, A&A, 557, A26
Martínez Pillet, V., Del Toro Iniesta, J. C., Álvarez-Herrero, A., et al. 2011, SoPh, 268, 57
Metcalf, T. R., Leka, K. D., Barnes, G., et al. 2006, SoPh, 237, 267
Pevtsov, A. A., Liu, Y., Virtanen, I., et al. 2021, JSWSC, 11, 14
Pomoell, J., Lumme, E., & Kilpua, E. 2019, SoPh, 294, 41
Rempel, M. 2014, ApJ, 789, 132
Rempel, M. 2017, ApJ, 834, 10
Rimmele, T. R., Warner, M., Keil, S. L., et al. 2020, SoPh, 295, 172
Schrijver, C. J., De Rosa, M. L., Metcalf, T. R., et al. 2006, SoPh, 235, 161
Shelyag, S., Mathioudakis, M., & Keenan, F. P. 2012, ApJL, 753, L22
Silva, S. S. A., Murabito, M., Jafarzadeh, S., et al. 2022, ApJ, 927, 146
Steiner, O., Rezaei, R., Schaffenberger, W., & Wedemeyer-Böhm, S. 2008, ApJL, 680, L85
Tremblay, B., & Attie, R. 2020, FrASS, 7, 25
Tremblay, B., Cossette, J.-F., Kazachenko, M. D., Charbonneau, P., & Vincent, A. 2021, JSWSC, 11, 9
Tremblay, B., Roudier, T., Rieutord, M., & Vincent, A. 2018, SoPh, 293, 57
Tziotziou, K., Georgoulis, M. K., & Liu, Y. 2013, ApJ, 772, 115
Ulrich, R. K. 1970, ApJ, 162, 993
Vernazza, J. E., Avrett, E. H., & Loeser, R. 1981, ApJS, 45, 635
Vögler, A., Shelyag, S., Schüssler, M., et al. 2005, A&A, 429, 335
Welsch, B. T. 2015, PASJ, 67, 18
Welsch, B. T., Abbett, W. P., De Rosa, M. L., et al. 2007, ApJ, 670, 1434
Welsch, B. T., & Fisher, G. H. 2016, Solar Physics, 291, 1681
Welsch, B. T., Fisher, G. H., & Sun, X. 2013, ApJ, 765, 98
Welsch, B. T., Kusano, K., Yamamoto, T. T., & Muglach, K. 2012, ApJ, 747, 130
Withbroe, G. L., & Noyes, R. W. 1977, ARA&A, 15, 363
Yadav, N., Cameron, R. H., & Solanki, S. K. 2020, ApJL, 894, L17
Yadav, N., Cameron, R. H., & Solanki, S. K. 2021, A&A, 645, A3
Yeates, A. R., Bianchi, F., Welsch, B. T., & Bushby, P. J. 2014, A&A, 564, A131